inorganics

MDPI

Article

Preparation of SBA-15-Supported Metals by Vapor-Phase Infiltration

Ching-Yu Wang, Kai Shen, Raymond J. Gorte and John M. Vohs *

Department of Chemical and Biomolecular Engineering, University of Pennsylvania, Philadelphia, PA 19104, USA
* Correspondence: vohs@seas.upenn.edu

Abstract: A simple method is presented for incorporating various catalytic metals into the pores of SBA-15 using vapor-phase infiltration. The precursors used in Atomic Layer Deposition (ALD) for Pt, Pd, Rh, Ru, and Ni were exposed to an evacuated SBA-15, resulting in monolayer films of the adsorbed precursors inside the mesopores. The metal particles that formed after removal of the precursor ligands remained in the pores and had particle sizes ranging from 3.8 nm for Pt to 5.2 nm for Ni, as determined by Transmission Electron Microscopy (TEM), XRD, and CO chemisorption. Metal loadings for saturation exposures ranged from 5.1-wt% for Ni to 9.1-wt% for Pt; however, uniform deposition was demonstrated for lower loadings of Pd by decreasing the amount of precursor. To determine the effect of the surface composition of the mesopores, Pd particles were also added to SBA-15 that was coated with a 0.2-nm film of ZrO_2.

Keywords: mesoporous silica; metal nanoparticle; atomic layer deposition (ALD); SBA-15; Pt; Pd; Rh; Ru; Ni

Citation: Wang, C.-Y.; Shen, K.; Gorte, R.J.; Vohs, J.M. Preparation of SBA-15-Supported Metals by Vapor-Phase Infiltration. *Inorganics* **2022**, *10*, 215. https://doi.org/10.3390/inorganics10110215

Academic Editor: Richard Walton

Received: 3 November 2022
Accepted: 17 November 2022
Published: 19 November 2022

1. Introduction

Mesoporous materials, such as SBA-15, are of interest as catalyst supports for transition metals due to their high surface areas and well-defined pore structures [1,2]. The mesoporous structure may prevent sintering of the supported metal nanoparticles due to the spatial isolation of the particles [3–5], may enhance selectivity for some reactions due to the molecular-sieving effect of the uniform pores [6,7], and may even suppress catalyst coking in some cases [8–10]. An interesting example that demonstrates the potential importance of having the catalyst particles within the mesopores comes from the work of Agirrezabal-Telleria et al., who studied ethene dimerization over Ni within Al-MCM-41 [8,9]. Coking was completely suppressed when the pressure was raised above that at which the ethene condensed in the pores due to the solvation of liquid-like ethene.

However, as demonstrated in several recent reviews [3,11], preparing catalysts in which the metal particles are all within the mesopores is challenging. Conventional incipient wetness approaches usually do not work because the impregnated metal salts are drawn out of the pores when the solvent is removed during the drying process. Alternative preparation methods broadly fall into three categories. In the first and most common method, deposition–precipitation, the metal is precipitated out of a supersaturated precursor solution within the pores prior to removal of the solvent [12,13]. The most common way of doing this involves changing the pH of the infiltrated solution, causing precipitation of the metal salts in the form of hydroxides [14]. A second method involves functionalizing the surface of the mesopores, then grafting the particles or precursors onto those surfaces [15,16]. Finally, one can synthesize the mesoporous material in a solution containing the catalyst nanoparticles so that the porous structure forms around the particles [17]. There are variations on these methods and some of these are described elsewhere [3,11,18–20]. Although successful methods for incorporating catalyst nanoparticles in the mesopores exist, these methods require multiple steps over a range of conditions and can be different

for each metal. A generally applicable method for efficiently incorporating metal particles in mesoporous materials is desirable.

We will show in this work that a wide range of metals, including Pt, Pd, Rh, Ru, and Ni, can be easily and quickly incorporated into SBA-15 by vapor-phase infiltration of metal precursors, using ideas from Atomic Layer Deposition (ALD). Depositing metals by this method on supports without mesopores has been reported previously [21–23]. In ALD, the vapor from a compound containing the metal of interest is allowed to react with a surface. After removing the excess precursor, the monolayer-covered surface is oxidized to remove the precursor ligands. Although the process can be repeated to increase the coverage, the metal loading associated with a monolayer of the precursor is usually sufficient.

2. Results and Discussion

A list of all the samples prepared in this study, along with a few key properties, is shown in Table 1. Except for the samples designated Pd/SBA-15(med) and Pd/SBA-15(low), all the samples received saturation exposures of the metal precursors. The metal loadings in this table are reported as both weight percent and metal atoms per area. The metal coverages in atoms/m^2 are the growth rates that would be obtained in one cycle of an ALD process. For unmodified SBA-15, the metal growth rates varied from a low of $3.6 \times 10^{17}/m^2$ for Pt to a high of $5.4 \times 10^{17}/m^2$ for Ni. These values are similar to the growth rates per cycle reported for a wide range of ALD precursors [24–29] and are close to the coverages expected for monolayers of the precursors on SBA-15. Interestingly, the area-specific Pd coverage was somewhat higher on Pd/ZrO_2/SBA-15 compared to Pd/SBA-15. Whether this is due to a change in the concentration of adsorption sites on ZrO_2 or the morphology of the ZrO_2 film is uncertain.

Table 1. Properties of SBA-15 and metal on SBA-15 synthesized by vapor-phase infiltration and WI.

Sample	Metal Loading (%)	Metal Coverage (Metal Atoms/m^2)	Surface Area (m^2/g)	Pore Volume (cm^3/g)
SBA-15	-	-	785	0.81
Pd/SBA-15	5.9	4.3×10^{17}	719	0.69
Pt/SBA-15	9.1	3.6×10^{17}	637	0.63
Ru/SBA-15	6.7	5.1×10^{17}	748	0.69
Rh/SBA-15	6.0	4.5×10^{17}	703	0.77
Ni/SBA-15	4.1	5.4×10^{17}	694	0.79
Pd/SBA-15(med)	3.8	2.8×10^{17}	686	0.67
Pd/SBA-15(low)	1.9	1.4×10^{17}	660	0.66
Pd/ZrO_2/SBA-15	Pd: 5.1 ZrO_2: 45.6	1.2×10^{18}	224	0.30
WI-Pd/SBA-15	1.0	-	563	0.62

The TEM images of Pd/SBA-15, Pt/SBA-15, Ru/SBA-15, Rh/SBA-15, and Ni/SBA-15 in Figure 1 demonstrate that the metal particles were uniformly distributed inside the mesopores of the SBA-15 in each case. The particle-size distributions, shown as insets in each of the micrographs, indicated average particle sizes of 4.9 nm for Pd, 3.8 nm for Pt, 4.3 nm for Ru, 5.0 nm for Rh, and 5.2 nm for Ni. These values are all less than the pore size of the SBA-15, determined from the isotherms to be 9.1 nm. The TEM results for the Pd-containing sample prepared by wet impregnation, WI-Pd/SBA-15, were dramatically different. Even though the Pd loading on the WI-Pd/SBA-15 was only 1-wt%, Figure 2 shows that most of the metal was in the form of large particles on the external surface of the SBA-15. We were not able to find any Pd particles within the mesopores of the sample.

A comparison of the TEM images of Pd/SBA-15(low) and Pd/SBA-15 in Figure 3 provides insight into how the metal particles form from the adsorbed precursors. The Pd particles in these two samples are similar in size, but the particles are farther apart in Pd/SBA-15(low). The similarity in the Pd particle size for different Pd loadings is

further demonstrated by the fact that the Pd dispersions, measured by CO adsorption, were essentially the same on the Pd/SBA-15, Pd/SBA-15(med), and SBA-15(low) as shown in Figure 4. The implications of these results are twofold. First, it demonstrates that, even with low loadings, we were able to adsorb the Pd precursor uniformly over the sample, since even for the Pd/SBA-15(low), the Pd particles were uniformly distributed over the entire SBA-15 sample and throughout the entire length of the mesopores. Second, formation of the metal particles must involve migration of the metal atoms within the mesopores and is likely limited by the size of the pore. Otherwise, one would expect the particle size to change with the loading, since the migration distance must be significantly different in these three samples.

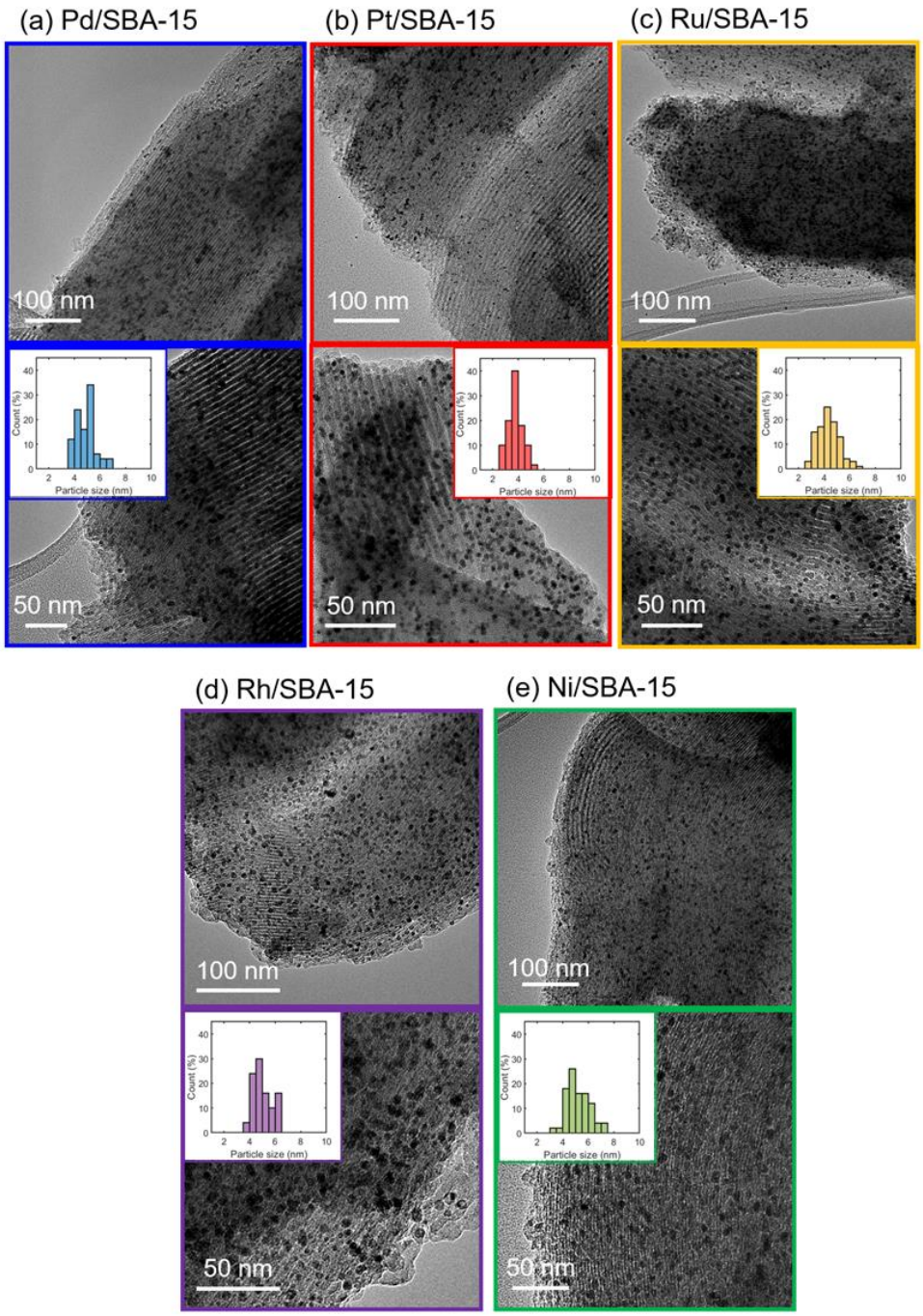

Figure 1. Representative TEM images of (**a**) Pd/SBA-15 (high loading), (**b**) Pt/SBA-15, (**c**) Ru/SBA-15, (**d**) Rh/SBA-15, and (**e**) Ni/SBA-15. The insets show the corresponding particle size distributions.

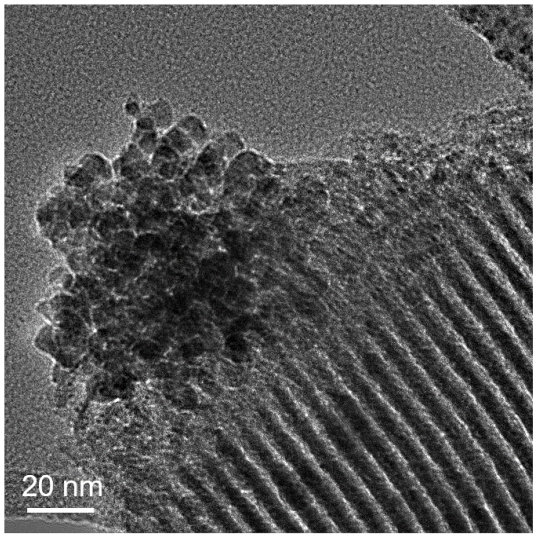

Figure 2. Representative TEM image of WI-Pd/SBA-15.

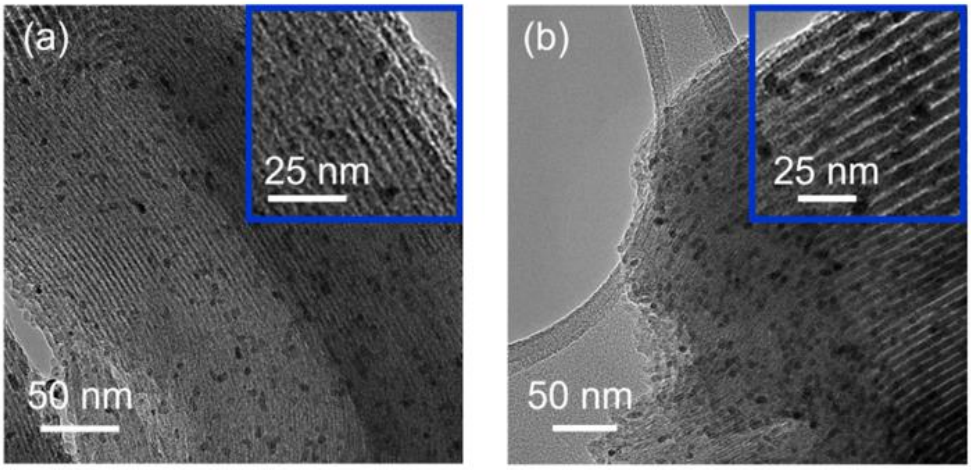

Figure 3. Representative TEM images of (**a**) Pd/SBA-15(low) and (**b**) Pd/SBA-15.

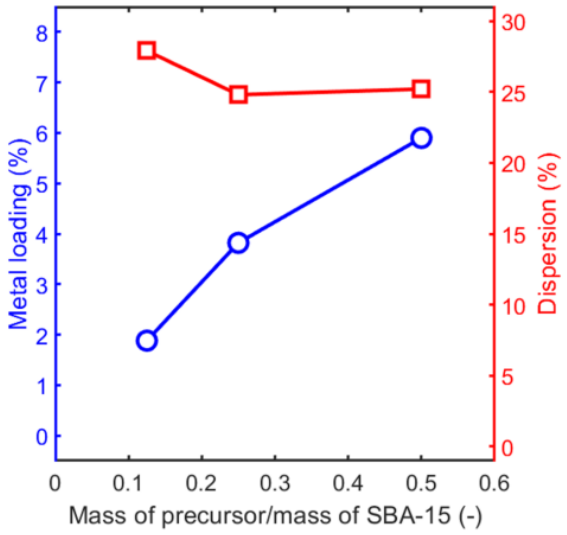

Figure 4. Pd loadings and dispersions versus the ratio of the mass of the precursor to the mass of the SBA-15.

It is also informative to consider the effect of the metal particles on the surface areas and pore morphologies. Table 1 shows that both the surface areas and pore volumes exhibited a modest decrease following the vapor-phase deposition of the metals. While the surface area of a given amount of SBA-15 is not expected to change with the addition of a small amount of metal, the surface area per gram of sample will change with the added mass. Because the densities of the metals are high, the volume of the metals is negligible compared to the volume of the pores. The surface area and pore volume decreased much more dramatically in the $Pd/ZrO_2/SBA\text{-}15$ due to the high coverage of ZrO_2.

However, closer examination of the isotherms in Figure 5 shows that the metal particles within the mesopores did affect the pore size distributions. This is most easily seen from the hysteresis loops in Figure 5a. For SBA-15, the loop existed over a narrow range of pressures and corresponded to an average pore size of 9.1 nm. Data for each of the metal-containing samples, with the possible exception of Ni/SBA-15, showed the loop extending to lower pressures. This corresponded to a decrease and slight broadening of the pore-size distribution. Since the total volume of the metal particles was not large, the effect on the pore size was relatively small, resulting in average pore sizes of 8.4 nm for Pd/SBA-15, 8.6 nm for Pt/SBA-15, 8.3 nm for Ru/SBA-15, 8.9 nm for Rh/SBA-15, and 8.9 nm for Ni/SBA-15.

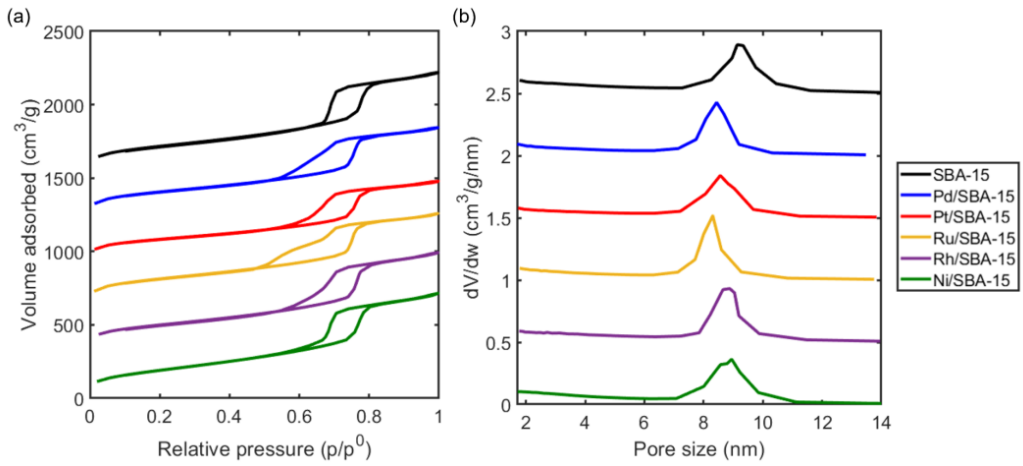

Figure 5. (**a**) N_2 adsorption–desorption isotherms and (**b**) pore size distributions of the SBA-15, Pd/SBA-15, Pt/SBA-15, Ru/SBA-15, Rh/SBA-15, and Ni/SBA-15.

X-Ray Diffraction (XRD) patterns of the Pd/SBA-15, Pt/SBA-15, Ru/SBA-15, Rh/SBA-15, and Ni/SBA-15 are reported in Figure 6 and were acquired to further characterize the metal particles. The SBA-15 showed no diffraction peaks at the angles shown because of the silica walls that made up the mesopores were amorphous. The peaks associated with the metal nanoparticles were visible for the Pd/SBA-15, Pt/SBA-15, and Rh/SBA-15 samples; but the peaks were broad, consistent with the small size of the particles. Based on the full width at half maximum and the Scherrer equation, the particles sizes for these three samples were 3.3 nm, 3.0 nm, and 4.8 nm, respectively. We were not able to observe the diffraction peaks for either Ru/SBA-15 or Ni/SBA-15.

The metal dispersions and particle sizes were also estimated from the chemisorption measurements performed at 298 K, assuming a stoichiometry of one CO per surface metal site. The results are shown in Table 2. The dispersions for Pd/SBA-15, Pt/SBA-15, and Rh/SBA-15 were between 21% and 25% respectively; the particle sizes calculated from these values agreed reasonably well with the values obtained from TEM and XRD. The dispersion values for Pd/SBA-15(low) and Pd/SBA-15(med) were similar to that of Pd/SBA-15, as discussed earlier; and the dispersion of the sample prepared by wet impregnation, WI-Pd/SBA-15, was very low, in agreement with the TEM data showing large metal particles. The dispersion obtained for Ru/SBA-15 was somewhat lower at 11%; we were not able to adsorb CO on Ni/SBA-15, possibly because of incomplete reduction.

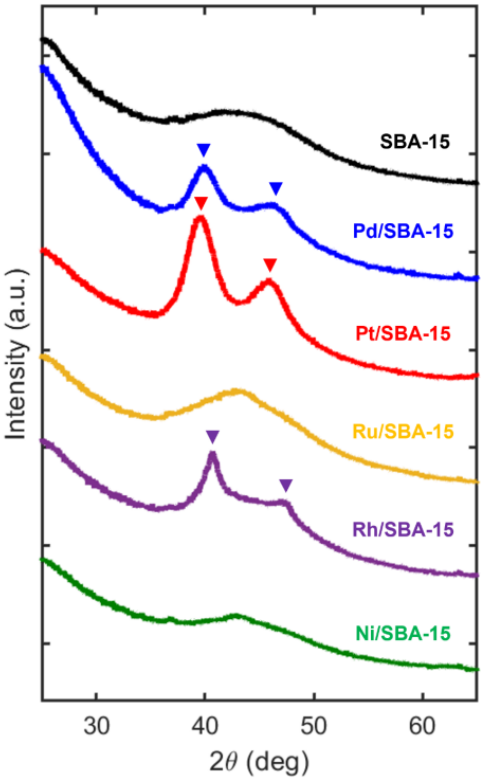

Figure 6. XRD patterns of SBA-15, Pd/SBA-15, Pt/SBA-15, Ru/SBA-15, Rh/SBA-15, and Ni/SBA-15. The blue, red, and purple triangles represent the characteristics peaks of the Pd, Pt, and Rh, respectively.

Table 2. Dispersions and average particles size of metal on SBA-15 synthesized by ALD and WI.

Sample	Dispersion Estimated from CO Chemisorption (%)	Particle Size [1] (nm)	Particle Size [2] (nm)	Particle Size [3] (nm)
Pd/SBA-15	25.2	4.4	3.3	4.9
Pt/SBA-15	24.1	4.7	3.0	3.8
Ru/SBA-15	11.3	11.4	n.m.	4.3
Rh/SBA-15	21.2	5.1	4.8	5.0
Ni/SBA-15	n.m.	n.m.	n.m.	5.2
Pd/SBA-15(med)	24.8	4.5	3.2	5.2
Pd/SBA-15(low)	27.9	4.0	2.8	5.0
Pd/ZrO2/SBA-15	32.1	3.5	n.m.	3.3
WI-Pd/SBA-15	3.2	34.8	n.m.	60

[1] Estimated from the dispersions with $D = 6\frac{v_m/a_m}{d_{va}}$. D, Vm, am, dva, represent the dispersion, volume of an atom, surface area of an atom, and average particle diameter, respectively. [2] Estimated from the full width at half maximum of the XRD peaks with the Scherrer equation. [3] Estimated from the TEM images. n.m.: not measurable.

Diffuse Reflectance Infrared Fourier Transform Spectra (DRIFTS) for the CO adsorption on the Pd/SBA-15, Pt/SBA-15, Ru/SBA-15, and Rh/SBA-15 are shown in Figure 7 and were again consistent with the metal particle sizes in the range from 3 to 5 nm. The spectra of the adsorbed CO showed both linear- and bridged-bonded CO on each of the metals, with the exception that Ru showed only the linear-bonded form. The presence of the bridge-bonded CO demonstrated that the spectra were not that of isolated metal atoms.

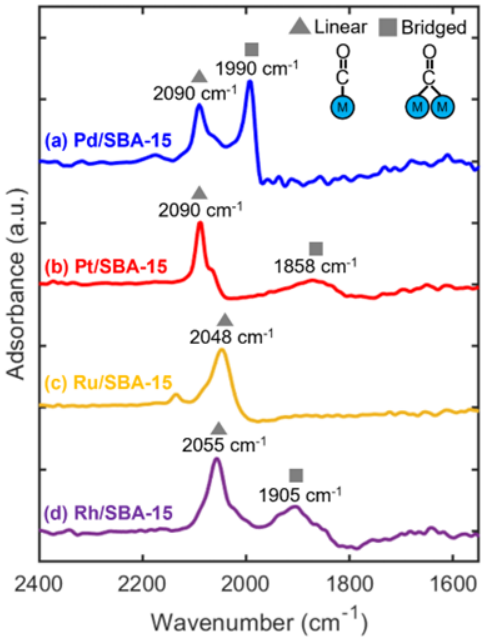

Figure 7. DRIFTS for the CO adsorption on the Pd/SBA-15, Pt/SBA-15, Ru/SBA-15, and Rh/SBA-15. The triangles and squares represent the linear- and bridged-bonded CO on the metals, respectively.

Silica is generally considered to be a weakly interacting support for most metal catalysts, and achieving and maintaining good dispersions with silica supports can sometimes be challenging [30]. To determine whether better dispersions might be achieved if the composition of the mesoporous walls were made of a different material, we deposited Pd onto SBA-15 that had been coated with 0.2 nm of ZrO_2 using ALD. The preparation of ZrO_2/SBA-15 has been described in detail elsewhere [24]. The thickness of the film was determined from the mass of ZrO_2 added (48 wt%), assuming the ZrO_2 uniformly covered the SBA-15 pores with its bulk density. Previous work also revealed that the pores of ZrO_2/SBA-15 were uniformly covered with ZrO_2, using temperature-programmed desorption of 2-propanol and the fact that ZrO_2 is more acidic than silica [24]. A saturation exposure of ZrO_2/SBA-15 to the Pd precursor resulted in a sample that had 5.1-wt% Pd, corresponding to a metal coverage of 1.2×10^{18} metal atoms/m^2. As discussed earlier, the higher Pd coverage on the Pd/ZrO_2/SBA-15 compared to the Pd/SBA-15 may be due to a higher adsorption-site density.

Representative TEM and scanning transmission electron microscopy (STEM) images with energy dispersive X-ray spectra (EDS) maps of Pd/ZrO_2/SBA-15 are reported in Figure 8. As in the case of Pd/SBA-15, the images show that the Pd nanoparticles in this sample were again aligned with the mesopores and of a similar size, 3.3 nm. The STEM image with EDS maps shows that the ZrO_2 and Pd nanoparticles were uniformly dispersed in the mesopores. Interestingly, the CO chemisorption measurements indicated that that the dispersion was slightly higher on this sample compared to the Pd/SBA, 15.32% versus 25%, even though the surface concentration of Pd was higher on the Pd/ZrO_2/SBA-15.

What we have demonstrated in this study is that vapor-phase infiltration provides a simple and highly flexible method for incorporating metal nanoparticles into mesoporous materials. Most of the metal added by simple wet-impregnation remained external to the mesopores but the vapor-phase infiltration resulted in a uniform distribution of the metal nanoparticles. While other methods have been developed for incorporating nanoparticles into the pores [3,11], most are either metal-specific or require multiple steps over a range of conditions. We successfully applied the vapor-phase infiltration to the addition of Pd, Pt, Ru, Rh, and Ni into SBA-15; extrapolation of the approach to other metals (e.g., Co [31], Fe [32]) and oxide (e.g., MnO_x [33]) catalysts would be a next step.

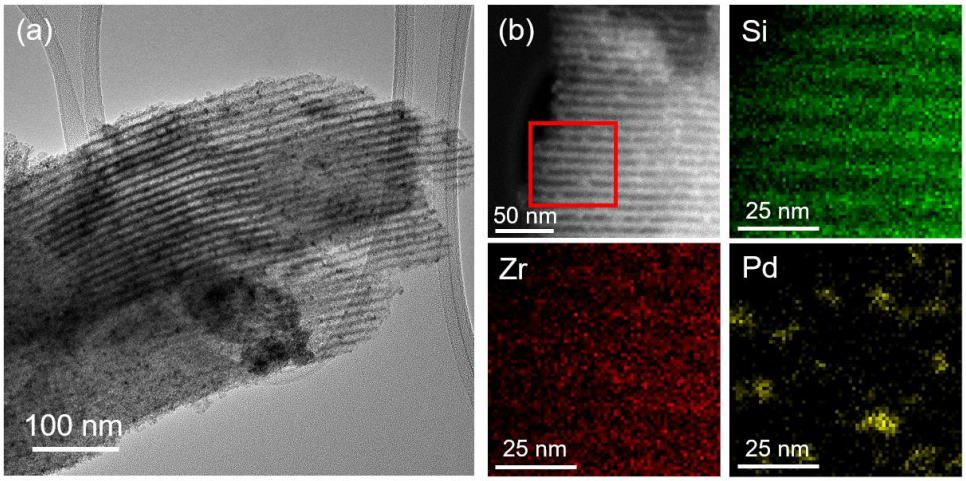

Figure 8. Representative (**a**) TEM and (**b**) STEM images with EDS maps of Pd/ZrO_2/SBA-15.

Obtaining high metal loadings by vapor-phase infiltration is relatively easy. Indeed, additional adsorption cycles could be used to increase the loading well above that achieved in the present study. Obtaining lower metal loadings may be more difficult in some cases, although we found that uniform distributions of Pd could be obtained using less of this specific precursor. Other precursors may adsorb chromatographically, either in the mouth of the mesopores or in the bed of powder. This issue would likely need to be addressed on a case-by-case basis.

3. Experimental Techniques

SBA-15 was synthesized following the procedure described in the literature [24,34]. First, 4.0 g of Pluronic P-123 (Sigma-Aldrich, St. Louis, MO, USA) was dissolved, with stirring, in a solution consisting of 120 g of 2 M HCl and 30 g of deionized water at 298 K for 20 h. Following dropwise addition of 8.5 g of tetraethoxysilane (TEOS, Sigma-Aldrich, 99%) at 308 K, the resulting liquid was maintained at the same temperature, with stirring for 20 h. Next, the solution was transferred to an autoclave, and the temperature was raised to 373 K for 24 h to facilitate the hydrolysis of TEOS. The resulting SBA-15 was filtered, washed with deionized water, and dried at 353 K. To remove the P-123 surfactant, the sample temperature was ramped at 1 K/min to 773 K in flowing air; then, it was held at that temperature for 6 h. The structure of the resulting SBA-15 was confirmed by the small-angle X-Ray Diffraction and STEM, as reported in a previous study [24].

The metals were added to SBA-15 by vapor-phase infiltration, using home-built equipment that was also used for ALD. The schematic diagram of the equipment is shown in the supporting information (See Figure S1). In the present study, approximately 0.2 g of SBA-15 was placed in a 10 mL quartz tube together with the desired amount of metal precursor. The tube could be evacuated to ~50 mTorr using a mechanical vacuum pump, isolated from the vacuum by a high-temperature valve, and then heated to a temperature sufficiently high to vaporize the metal precursor. In a typical experiment, the SBA-15 was exposed to the precursor vapor for 10 min, after which the sample was again evacuated at the exposure temperature. In order to measure the growth rates, most of the experiments in this study used approximately 50% more precursor than that required to form a monolayer, with the excess precursor simply removed during the evacuation step; however, additional experiments were performed with lower amounts of Pd precursor to determine whether uniform deposition could be achieved at lower metal coverages. Multiple batches were prepared for some of the samples, and the results were identical in each case. To determine the effect of substrate composition, Pd was also added to an SBA-15 sample that had been modified by a 0.2 nm film (48 wt%) of ZrO_2. The film was added by ALD, and the sample and its preparation have been described in detail in a previous publication [24].

The precursors used for the deposition of Pd, Pt, Ru, Rh, and Ni were bis(2,2,6,6-tetramethyl-3,5-heptanedionato)palladium ($Pd(TMHD)_2$, Strem Chemicals, Newburyport, MA, USA, >98%), platinum acetylacetonate ($Pt(acac)_2$, Strem Chemicals, 98%), tris(2,2,6,6-tetramethyl-3,5-heptanedionato)ruthenium ($Ru(TMHD)_3$, Strem Chemicals, 99%), rhodium acetylacetonate ($Rh(acac)_3$, Strem Chemicals, >97%), and bis(2,2,6,6-tetramethyl-3,5-heptanedionato)nickel ($Ni(TMHD)_2$, Strem Chemicals, >98%). The exposure temperatures, chosen in order to achieve a sufficient vapor pressure without decomposition of the precursors, were 443 K for Pt, 473 K for Rh, and 523 K for Pd, Ru, and Ni. After deposition, the samples exposed to the precursors of Pd, Pt, Rh, and Ni were removed from the adsorption system, calcined in flowing air at 773 K for 20 min to remove the ligands, and then reduced in flowing H_2 for 20 min at 573 K. Because RuO_4 has a high vapor pressure, the ligands on the Ru-containing sample were removed by heating the sample in a flowing H_2 at 623 K.

For comparison purposes, Pd was also incorporated with SBA-15 using wet impregnation. SBA-15 was initially added to an aqueous solution containing palladium nitrate dihydrate ($Pd(NO_3)_2 \cdot 2H_2O$, Pd 4.501% *w/w*, Alfa Aesar, Haverhill, MA, USA) with stirring for 2 h. The sample was then dried at 343 K in air overnight, followed by calcination at 773 K in flowing air for 2 h.

The metal loadings in this study were determined from the sample weight changes. All the samples were reduced at 573 K or 623 K (for Ru/SBA-15) before performing characterization. N_2 adsorption–desorption isotherms were measured at 78 K using a Micromeritics, TriStar II Plus analyzer. The surface areas were determined from BET isotherms, with pore-size distributions calculated using the Barret–Joyner–Halenda (BJH) method. Metal dispersions were measured using CO chemisorption at 298 K, assuming a stoichiometry of one CO molecule per surface site. XRD patterns were obtained using a Rigaku MiniFlex 6G X-ray diffractometer. TEM, STEM, and EDS were performed with a JEOL JEM-F200 STEM operated at 200 kV. For these measurements, the samples were diluted in ethanol and then deposited onto carbon support films on copper grids (Electron Microscopy Sciences, Hatfield, PA, USA). DRIFTS were performed using an IR spectrometer (Mattson, Galaxy, Mattson Technology, Fremont, CA, USA) equipped with a diffuse-reflectance cell (Pike Technologies, DiffusIR, Fitchburg, WI, USA). In each DRIFTS measurement, the sample was pretreated at 573 K with flowing H_2/He for 30 min before cooling to 373 K. The sample was then exposed to CO for 10 min before flushing the excess CO from the system with flowing He for 10 min. All DRIFTS results were collected with the sample at 373 K.

4. Conclusions

In this paper, we demonstrated that various catalytic metals could be incorporated into the mesopores of SBA-15 by exposing the evacuated SBA-15 to vapors of ALD precursors. The method is simple, quick, and applicable to a wide range of metals and mesoporous materials. The amount of metal that was added to the SBA-15 depended on the precursor exposure, but high metal loadings could be easily achieved.

Supplementary Materials: The following supporting information can be downloaded at: https://www.mdpi.com/article/10.3390/inorganics10110215/s1. Figure S1: Schematic diagram of the home-built vapor-phase infiltration equipment.

Author Contributions: Investigation, C.-Y.W. and K.S.; writing—original draft preparation, C.-Y.W.; writing—review and editing, R.J.G. and J.M.V. All authors have read and agreed to the published version of the manuscript.

Funding: This work was funded by the Department of Energy, Office of Basic Energy Sciences, Chemical Sciences, Geosciences and Biosciences Division, Grant No. DE-FG02-13ER16380. The STEM work was carried out in part at the Singh Center for Nanotechnology, which is supported by the National Science Foundation grant NNCI-1542153.

Data Availability Statement: The data presented in this study are available on request from the corresponding author.

Conflicts of Interest: The authors declare no conflict of interest.

References

1. Verma, P.; Kuwahara, Y.; Mori, K.; Raja, R.; Yamashita, H. Functionalized mesoporous SBA-15 silica: Recent trends and catalytic applications. *Nanoscale* **2020**, *12*, 11333–11363. [CrossRef] [PubMed]
2. Gao, C.B.; Lyu, F.L.; Yin, Y.D. Encapsulated Metal Nanoparticles for Catalysis. *Chem. Rev.* **2021**, *121*, 834–881. [CrossRef] [PubMed]
3. Singh, S.; Kumar, R.; Setiabudi, H.D.; Nanda, S.; Vo, D.V.N. Advanced synthesis strategies of mesoporous SBA-15 supported catalysts for catalytic reforming applications: A state-of-the-art review. *Appl. Catal. A-Gen.* **2018**, *559*, 57–74. [CrossRef]
4. Lyu, X.; Wu, X.; Liu, Y.Z.; Huang, W.Y.; Lee, B.Y.D.; Li, T. Synthesis and Characterization of Mesoporous Silica Nanoparticles Loaded with Pt Catalysts. *Catalysts* **2022**, *12*, 183. [CrossRef]
5. Naik, P.J.; Chatterjee, P.; Chen, S.J.; Huang, W.Y.; Slowing, I.I. Regulating the Catalytic Activity of Pd Nanoparticles by Confinement in Ordered Mesoporous Supports. *ChemCatChem* **2021**, *13*, 539–542. [CrossRef]
6. Cejka, J.; Mintova, S. Perspectives of micro/mesoporous composites in catalysis. *Catal. Rev.-Sci. Eng.* **2007**, *49*, 457–509. [CrossRef]
7. Pump, E.; Cao, Z.; Samantaray, M.K.; Bendjeriou-Sedjerari, A.; Cavallo, L.; Basset, J.M. Exploiting Confinement Effects to Tune Selectivity in Cyclooctane Metathesis. *ACS Catal.* **2017**, *7*, 6581–6586. [CrossRef]
8. Agirrezabal-Telleria, I.; Iglesia, E. Stabilization of active, selective, and regenerable Ni-based dimerization catalysts by condensation of ethene withinordered mesopores. *J. Catal.* **2017**, *352*, 505–514. [CrossRef]
9. Agirrezabal-Telleria, I.; Iglesia, E. Mechanistic insights and consequences of intrapore liquids in ethene, propene, and butene dimerization on isolated Ni^{2+} sites grafted within aluminosilicate mesopores. *J. Catal.* **2020**, *389*, 690–705. [CrossRef]
10. Zhang, H.C.; Xiao, Z.R.; Yang, M.; Zou, J.J.; Liu, G.Z.; Zhang, X.W. Highly dispersible cerium-oxide modified Ni/SBA-15 for steam reforming of bio-mass based JP10. *Chin. J. Chem. Eng.* **2022**, *43*, 255–265. [CrossRef]
11. Zhang, W.; Zhu, K.R.; Ren, W.X.; He, H.L.; Liang, H.C.; Zhai, Y.P.; Li, W. Recent Advances in the Marriage of Catalyst Nanoparticles and Mesoporous Supports. *Adv. Mater. Interfaces* **2022**, *9*, 2101528. [CrossRef]
12. Chytil, S.; Glomm, W.R.; Blekkan, E.A. Characterization of Pt/SBA-15 prepared by the deposition-precipitation method. *Catal. Today* **2009**, *147*, 217–223. [CrossRef]
13. Rodriguez-Gomez, A.; Pereniguez, R.; Caballero, A. Understanding the differences in catalytic performance for hydrogen production of Ni and Co supported on mesoporous SBA-15. *Catal. Today* **2018**, *307*, 224–230. [CrossRef]
14. Jung, S.W.; Lu, C.; He, H.P.; Ahn, K.Y.; Gorte, R.J.; Vohs, J.M. Influence of composition and Cu impregnation method on the performance of $Cu/CeO_2/YSZ$ SOFC anodes. *J. Power Source* **2006**, *154*, 42–50. [CrossRef]
15. Yang, C.M.; Sheu, H.S.; Chao, K.J. Templated synthesis and structural study of densely packed metal nanostructures in MCM-41 and MCM-48. *Adv. Funct. Mater.* **2002**, *12*, 143–148. [CrossRef]
16. Jiao, L.; Regalbuto, J.R. The synthesis of highly dispersed noble and base metals on silica via strong electrostatic adsorption: II. Mesoporous silica SBA-15. *J. Catal.* **2008**, *260*, 342–350. [CrossRef]
17. Wang, S.; Zhao, Q.F.; Wei, H.M.; Wang, J.Q.; Cho, M.Y.; Cho, H.S.; Terasaki, O.; Wan, Y. Aggregation-Free Gold Nanoparticles in Ordered Mesoporous Carbons: Toward Highly Active and Stable Heterogeneous Catalysts. *J. Am. Chem. Soc.* **2013**, *135*, 11849–11860. [CrossRef]
18. Zhu, J.J.; Wang, T.; Xu, X.L.; Xiao, P.; Li, J.L. Pt nanoparticles supported on SBA-15: Synthesis, characterization and applications in heterogeneous catalysis. *Appl. Catal. B-Environ.* **2013**, *130*, 197–217. [CrossRef]
19. Sietsma, J.R.A.; Meeldijk, J.D.; den Breejen, J.P.; Versluijs-Helder, M.; van Dillen, A.J.; de Jongh, P.E.; de Jong, K.P. The preparation of supported NiO and Co_3O_4 nanoparticles by the nitric oxide controlled thermal decomposition of nitrates. *Angew. Chem.-Int. Edit.* **2007**, *46*, 4547–4549. [CrossRef] [PubMed]
20. Ungureanu, A.; Chirieac, A.; Ciotonea, C.; Mazilu, I.; Catrinescu, C.; Petit, S.; Marceau, E.; Royer, S.; Dumitriu, E. Enhancement of the dispersion and catalytic performances of copper in the hydrogenation of cinnamaldehyde by incorporation of aluminium into mesoporous SBA-15 silica. *Appl. Catal. A-Gen.* **2020**, *598*, 117615. [CrossRef]
21. Huang, R.J.; Kwon, O.; Lin, C.; Gorte, R.J. The effects of SMSI on m-Cresol hydrodeoxygenation over Pt/Nb_2O_5 and Pt/TiO_2. *J. Catal.* **2021**, *398*, 102–108. [CrossRef]
22. Cao, T.; Wang, C.-Y.; Shen, K.; Vohs, J.M.; Gorte, R.J. Investigation into support effects for Pt and Pd on $LaMnO_3$. *Appl. Catal. A Gen.* **2022**, *646*, 118873. [CrossRef]
23. Lin, C.; Foucher, A.C.; Ji, Y.C.; Stach, E.A.; Gorte, R.J. Investigation of Rh-titanate ($ATiO_3$) interactions on high-surface-area perovskite thin films prepared by atomic layer deposition. *J. Mater. Chem. A* **2020**, *8*, 16973–16984. [CrossRef]
24. Wang, C.Y.; Kwon, O.; Gorte, R.J.; Vohs, J.M. Synthesis of high-surface area tungstated zirconia by atomic layer deposition on mesoporous silica. *Microporous Mesoporous Mat.* **2022**, *335*, 111821. [CrossRef]
25. Kwon, O.; Huang, R.J.; Cao, T.Y.; Vohs, J.M.; Gorte, R.J. Dry reforming of methane over Ni supported on $LaMnO_3$ thin films. *Catal. Today* **2021**, *382*, 142–147. [CrossRef]
26. Onn, T.M.; Zhang, S.Y.; Arroyo-Ramirez, L.; Chung, Y.C.; Graham, G.W.; Pan, X.Q.; Gorte, R.J. Improved Thermal Stability and Methane-Oxidation Activity of Pd/Al_2O_3 Catalysts by Atomic Layer Deposition of ZrO_2. *ACS Catal.* **2015**, *5*, 5696–5701. [CrossRef]
27. Lin, C.; Foucher, A.C.; Ji, Y.C.; Curran, C.D.; Stach, E.A.; McIntosh, S.; Gorte, R.J. "Intelligent" Pt Catalysts Studied on High-Surface-Area $CaTiO_3$ Films. *ACS Catal.* **2019**, *9*, 7318–7327. [CrossRef]

28. Puurunen, R.L. Surface chemistry of atomic layer deposition: A case study for the trimethylaluminum/water process. *J. Appl. Phys.* **2005**, *97*, 121301. [CrossRef]
29. Ke, W.; Liu, Y.; Wang, X.L.; Qin, X.D.; Chen, L.M.; Palomino, R.M.; Simonovis, J.P.; Lee, I.; Waluyo, I.; Rodriguez, J.A.; et al. Nucleation and Initial Stages of Growth during the Atomic Layer Deposition of Titanium Oxide on Mesoporous Silica. *Nano Lett.* **2020**, *20*, 6884–6890. [CrossRef] [PubMed]
30. Soled, S. Case Studies of Nobel-Metal Catalysts. In *Synthesis of Solid Catalysts*; de Jong, K.P., Ed.; John Wiley & Sons, Ltd.: New York, NY, USA, 2009; pp. 353–367.
31. Huang, R.J.; Cheng, Y.; Ji, Y.C.; Gorte, R.J. Atomic Layer Deposition for Preparing Isolated Co Sites on SiO_2 for Ethane Dehydrogenation Catalysis. *Nanomaterials* **2020**, *10*, 244. [CrossRef] [PubMed]
32. Onn, T.M.; Monai, M.; Dai, S.; Arroyo-Ramirez, L.; Zhang, S.Y.; Pan, X.Q.; Graham, G.W.; Fornasiero, P.; Gorte, R.J. High-surface-area, iron-oxide films prepared by atomic layer deposition on gamma-Al_2O_3. *Appl. Catal. A-Gen.* **2017**, *534*, 70–77. [CrossRef]
33. Lee, S.; Lin, C.; Kim, S.; Mao, X.Y.; Kim, T.; Kim, S.J.; Gorte, R.J.; Jung, W. Manganese Oxide Overlayers Promote CO Oxidation on Pt. *ACS Catal.* **2021**, *11*, 13935–13946. [CrossRef]
34. Zhao, D.Y.; Feng, J.L.; Huo, Q.S.; Melosh, N.; Fredrickson, G.H.; Chmelka, B.F.; Stucky, G.D. Triblock copolymer syntheses of mesoporous silica with periodic 50 to 300 angstrom pores. *Science* **1998**, *279*, 548–552. [CrossRef] [PubMed]